



Discrete element parameter calibration and the modelling of dragline bucket filling

C.J. Coetzee*, D.N.J. Els, G.F. Dymond

Department of Mechanical and Mechatronic Engineering, Stellenbosch University, Stellenbosch, South Africa

Received 5 May 2008; received in revised form 5 March 2009; accepted 31 March 2009

Abstract

The Discrete Element Method (DEM) is useful for modelling granular flow. The accuracy of DEM modelling is dependent upon the model parameter values used. Determining these values remains one of the main challenges. In this study a method for determining the parameters of cohesionless granular material is presented. The particle size and density were directly measured and modelled. The particle shapes were modelled using two to four spheres clumped together. The remaining unknown parameter values were determined using confined compression tests and angle of repose tests. This was done by conducting laboratory experiments followed by equivalent numerical experiments and iteratively changing the parameters until the laboratory results were replicated. The modelling results of the confined compression tests were mainly influenced by the particle stiffness. The modelling results of the angle of repose tests were dependent on both the particle stiffness and the particle friction coefficient. From these observations, the confined compression test could be used to determine the particle stiffness and with the stiffness known, the angle of repose test could be used to determine the particle friction coefficient. Usually DEM codes do not solve the equations of motion for so-called walls (non-granular structural elements). However, in this study a dynamic model of a dragline bucket is developed and implemented in a commercial DEM code which allows the dynamics of the walls to be modelled. The DEM modelling of large systems of particles is still a challenge and procedures to simplify and speed up the modelling of dragline bucket filling are presented. Using the calibrated parameters, numerical results of bucket filling are compared to experimental results. The model accurately predicted the orientation of the bucket. The model also accurately predicted the drag force over the first third of the drag, but predicted drag forces too high for the subsequent part of the drag.

© 2009 ISTVS. Published by Elsevier Ltd. All rights reserved.

1. Introduction

In open cast mining, the overburden needs to be removed in order to mine the ore below. This overburden can vary from topsoil to hard rock. The bulk of the costs involved in open cast mining can be attributed to overburden removal.

Draglines are very economical and represent the most popular of all overburden removal devices. They are usually used in combination with scrapers to reduce the amount of re-handle. A dragline is a crane-like structure with a large bucket of up to 100 m³ in volume, suspended

by steel ropes (Fig. 1). The bucket is dragged through the overburden and once the bucket has been filled, it is hoisted up. The base of the dragline pivots and the overburden is dumped elsewhere. The overburden usually needs to be blasted before the dragline can be used.

Draglines are designed to operate 24 h a day for 360 days a year. The cost of the loss of production due to dragline down time has been estimated at 8000 Australian dollars an hour [8]. Many dragline breakdowns can be attributed to the design of the bucket. The buckets either fail or overload the machine and cause failures in the dragline boom and main structure.

The filling of a bucket is a complex granular flow problem. Instrumentation of equipment for quantifying certain parameters of the operation is difficult and expensive. It is possible to use small-scale (usually 1/10th scale)

* Corresponding author. Tel.: +27 0 21 808 4239; fax: +27 0 21 808 4958.

E-mail address: ccoetzee@sun.ac.za (C.J. Coetzee).

Nomenclature

\bar{a}	rotation axis	V_r	rope drag speed over the winch
\bar{E}_S^R	rotation matrix from base S to base R	$\dot{\bar{x}}_{GS}$	velocity vector of the bucket's centre-of-gravity in base S
\bar{F}_{GS}	bucket body force	$\ddot{\bar{x}}_{GS}$	acceleration vector of the bucket's centre-of-gravity in base S
\bar{F}_{iS}	resultant force vector on wall i due to particle interaction	\bar{x}_{hR}	position vector of the hitch point relative to G in base R
F_n	contact force in the normal direction	$\dot{\bar{x}}_{hS}$	velocity vector of the hitch point in base S
$\bar{F}_{r1S}, \bar{F}_{r2S}$	drag force in rope 1 and rope 2, respectively	$\bar{x}_{h1S}, \bar{x}_{h2S}$	position vector of the hitch points relative to G
F_s	contact force in the shear direction	\bar{x}_{pR}	position vector of point p relative to G in base R
G	bucket's centre-of-gravity	$\dot{\bar{x}}_{pS}$	velocity vector of an arbitrary point p in base S
\bar{I}	inertia tensor	\bar{x}_w	unit vector pointing from the hitch point towards the winch
\bar{I}_d	identity matrix	ΔL_h	hitch point movement in direction of the rope in a single time step
k_n	stiffness in the contact normal direction	ΔL_w	change in drag rope length
k_r	stiffness of the drag rope	ϕ	rotation angle
k_s	stiffness in the contact shear direction	μ	contact friction coefficient
m_i	mass of wall i	\bar{p}	quaternion
\bar{M}_{iS}	resultant moment vector acting on wall i due to particle interaction	$\bar{\omega}_{GR}$	rotational bucket velocity vector in base R
\bar{M}_R	resultant moment acting on the bucket	$\ddot{\bar{\omega}}_{GR}$	rotational bucket acceleration vector in base R
R	rotating (attached to the bucket) coordinate system		
S	static (global) coordinate system		
t	time		
U_n	contact overlap in the normal direction		
U_s	contact overlap in the shear direction		

experimental rigs to evaluate bucket designs [10,23] but they are expensive and there are questions regarding the validity of scaling [21,22]. To scale-up results from model experiments is problematic since there are no general scaling laws for granular flows [6].

Numerical models and simulations have become an important design tool in engineering. Although numerical simulations seldom totally replace experiments, they allow designers to investigate a far wider range of options in a relatively short time and usually at much lower cost than using experimental investigations. A sensitivity analysis to determine the influence of specific parameters on the performance can be done more easily and comprehensively. Expensive experiments can then be used after numerical investigations to “fine tune” the design [17].

The Discrete Element Method (DEM) has been used to predict the behaviour of granular materials for the last two decades. A DEM code was first developed by [7] to simulate rock fracture mechanics. Today, there are commercial DEM codes available in both two and three dimensions. DEM is based on the simulation of the motion of granular material as separate particles. Calculations performed during a DEM simulation alternate between the application of Newton's second law to the particles and a force-displacement law at the inter-particle contacts. DEM has the advantage that it can easily be used for the simulation of granular flow subjected to large deformations and free

boundaries. With the development of faster computers, the number of particles that can be simulated has increased, allowing for more accurate material representation and the modelling of large industrial processes. The main problem with DEM is how to specify the micro-parameters (particle size, shape and contact parameters) so that the flow on macro-level of thousands of particles behaves in the same way as real granular flow. Laboratory experiments [11] or in situ tests [3] are necessary to determine these parameters before any useful modelling can be performed and valid predictions can be made.

In order to accurately model dragline bucket filling, both the granular material and the bucket dynamics must be accurately modelled. A dragline bucket is suspended by ropes and the motion of the bucket is influenced by the forces acting on it (gravity, rope forces and the interaction forces with the soil). The path followed by the bucket and the bucket's orientation is not known in advance or manipulated by the operator, as in the case of hydraulic excavators for example. The dragline operator positions the bucket on the ground and then the bucket is dragged in the general direction of the drag ropes at constant rope speed.

In a DEM model, structures such as buckets are modelled using walls. DEM codes calculate the behaviour of the particles based on the forces acting on them, but most DEM codes do not solve the equations of motion for the

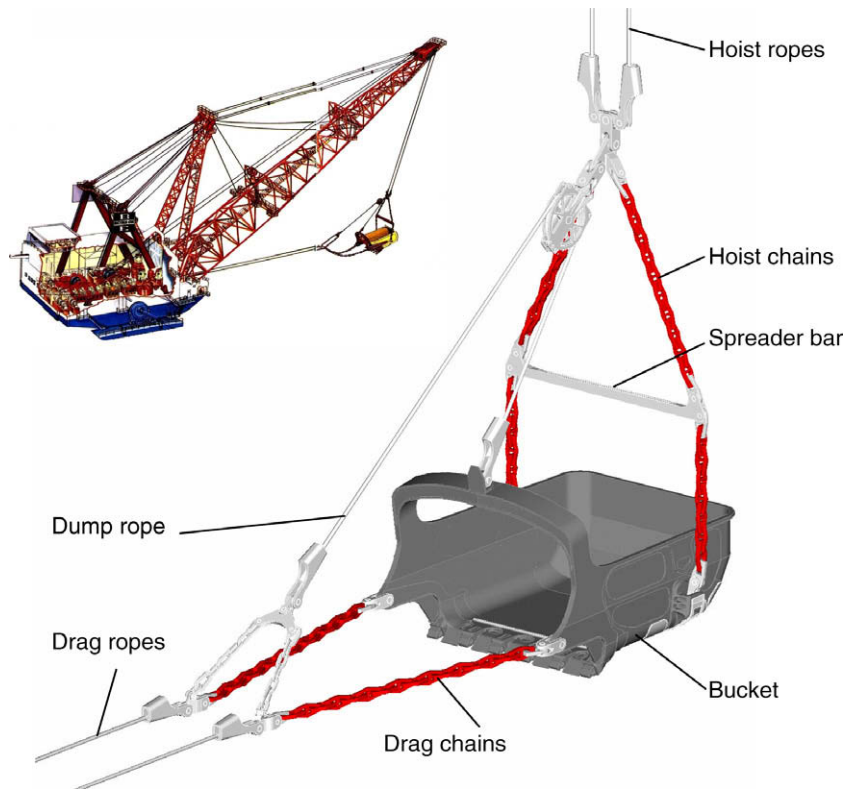


Fig. 1. A typical walking dragline and the bucket rigging (VR Steel).

walls. In some DEM codes, the translational and rotational velocity of the walls cannot be changed during the simulation, or the velocity can only be pre-programmed as a function of time. In dragline bucket modelling the velocity of the walls (bucket) needs to change according to the forces acting on it and it cannot be pre-programmed.

The DEM codes by Itasca give the user access to almost all internal variables via the built-in programming language, FISH. This feature makes it possible to obtain the resultant force and moment caused by particles on a wall. The resultant force and moment vectors can then be used to solve the equations of motion for each wall and update the velocity of each wall accordingly. In this paper, this option is used to model the dynamic behaviour of a dragline bucket.

Commercial DEM codes include general purpose codes such as *PFC^{2D}*, *PFC^{3D}*, *UDEC*, *3DEC* ([14]), *EDEM* ([9]), *Newton* [1], *Elfen* ([24]), *Bulk Flow Analyst* [2] and codes for specific applications such as *Chute Analyst* ([20]) and *Chute Maven* ([4]). In this paper, *PFC^{3D}* is used.

Discrete element modelling of dragline bucket filling has never been directly compared to experimental results. Cleary [6] modelled dragline bucket filling and trends were shown and qualitative comparisons made, but no experimental results were presented.

This paper addresses the challenges in the DEM modelling of dragline buckets, namely accurate modelling of material properties and the modelling of the bucket dynamics. The experimental setup and numerical model

are described followed by a comparison between the experimental and numerical results.

2. The Discrete Element Method

Discrete Element Methods are based on the simulation of the motion of granular material as separate particles [7]. Using the soft particle approach, each contact is modelled with a linear spring in the contact normal direction (secant stiffness k_n) and a linear spring in the contact tangential direction (tangent stiffness k_s) as depicted in Fig. 2. Frictional slip is allowed in the tangential direction with a friction coefficient μ . The particles are allowed to overlap and the amount of overlap is used in combination with the spring stiffness to calculate the contact force components. The contact force in the normal direction is given by

$$F_n = - \sum k_n U_n \quad (1)$$

where U_n is the overlap in the contact normal direction. The contact shear force is given by

$$F_s = \begin{cases} \sum k_s \Delta U_s & \text{for } |F_s| < |\mu F_n| \\ \mu F_n \text{sign}(\sum \Delta U_s) & \text{for } |F_s| \geq |\mu F_n| \end{cases} \quad (2)$$

where ΔU_s is the displacement increment in the contact tangential direction. This is the basic linear contact model as found in most DEM codes. Non-linear models [12,19,27] are also available, but are usually computationally less efficient. In general, cohesion can be modelled using bonds at

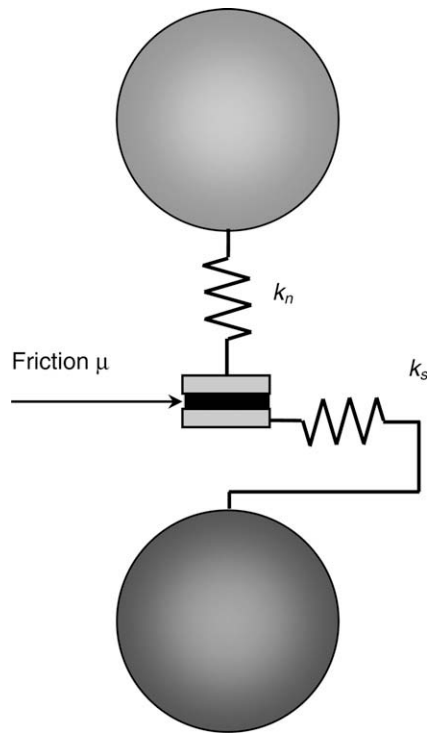


Fig. 2. Typical DEM particle contact model.

contacts. In this study only cohesionless material is considered and bonds are not needed. For a detailed description of DEM, the reader is referred to [7,5,13,28].

Using spherical particles, the internal friction of the material (assembly of particles) is usually too low when compared to real granular material like crushed rock. Non-spherical particles are needed to increase the particle interlocking effect and one solution is to make use of clumped particles. Clumps can be formed by adding two or more spherical particles together to form one rigid particle, i.e. particles comprising the clump remain at a fixed distance from each other [15]. Particles within a clump can overlap to any extent and contact forces are not generated between these particles. Clumps cannot break up during simulations regardless of the forces acting upon them. Asaf [3] investigated the effect of particle structure on internal friction angle. They used two equally sized discs,

clumped together, and biaxial tests to investigate the effect of particle centre distance on the internal friction angle. Results showed that the internal friction increases with an increase in the centre distance with an asymptotic behaviour. It was noticeable that beyond a certain centre distance, the value of the internal friction remained relatively constant although the centre distance is increased.

3. Experimental setup

A scale dragline model was built to obtain data which could be used to validate the numerical results. The drag forces, the bucket trajectory (path) and the bucket's orientation during a filling cycle were recorded.

The bucket was a 1:18 scale model of a 61 m³ bucket ([26]). The bucket had a length and width of roughly 300 mm and a fill height of 175 mm (Fig. 3). The size of the drag bed was determined by the size of the bucket used. The width and height were chosen to minimise boundary effects. The bed had a width of three times the bucket width and a length of 10 times the bucket length and filled with material three times the bucket height. The drag bed included means of attaching the sensors and was designed to be inclined which allowed different drag angles to be tested. Crushed rock from a roller mill with 25 mm of clearance between the rollers was used (Fig. 4).

The bucket was dragged at constant rope speed using a hydraulic cylinder in conjunction with a servo valve. The cylinder speed was measured by means of a linear variable differential transducer. The drag force was measured using a calibrated commercial load cell on each rope.

Three cable displacement sensors (ASM W12) were used to determine the three-dimensional position of a point on the bucket. The body of each sensor was attached to the rig frame, with the end of each cable attached to the centre of the bucket arch (Fig. 5). Using a triangulation algorithm, the position of the arch point could be determined. The three sensors were placed in a plane parallel to the drag bed and positioned to maximise the angle between sensors. The bucket's orientation (angle) was measured using a three axis inclinometer (Micro-Strain 3DM-G). This sensor was also attached to the arch of the bucket. Data were collected at 25 Hz using a data logger (HBM spider 8–30).

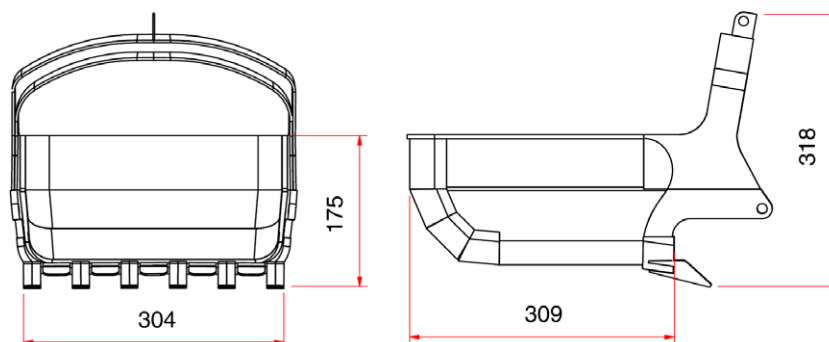


Fig. 3. Scale bucket basic dimensions in millimetre.



Fig. 4. Crushed rock used in the experiments.

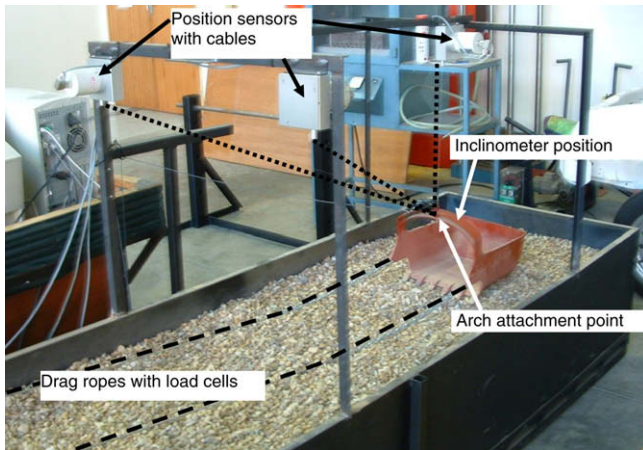


Fig. 5. Experimental setup showing the position of the sensors.

4. Material calibration

This section discusses the methods used to determine the granular material parameters. In order to fully describe the cohesionless material in PFC^{3D} , the following material properties were needed:

- particle shape distribution,
- particle size distribution,
- density,
- normal and shear stiffness and
- friction coefficient.

4.1. Particle shape distribution

The material used to simulate the overburden in the experimental setup was crushed rock from a roller mill with a 25 mm of clearance between the rollers. A random sample of 300 rocks was taken and the rocks could be classified

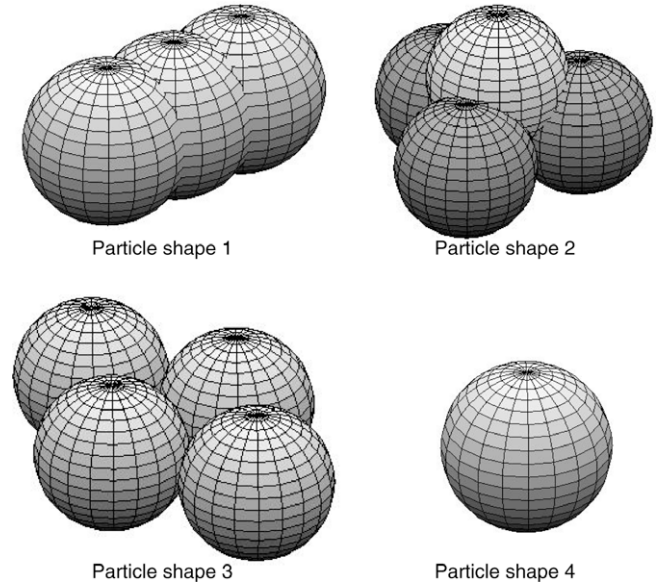


Fig. 6. Simplified particle shapes used in DEM model.

into four distinct particle shapes. These shapes were kept as simple as possible, while ensuring that every rock in the sample belonged to one of the particle shapes. The particle shapes were (Fig. 6):

- Shape 1: long rectangular particle comprising three aligned spheres (length to width ratio of clumped particle greater than 2).
- Shape 2: pyramid shape particle comprising four spheres.
- Shape 3: flat particle comprising four spheres (length to width ratio of clumped particle less than two, and ratio between length and height greater than 2).
- Shape 4: spherical particles comprising one sphere.

The rock sample was classified according to the above shapes. The number of particles belonging to each shape was recorded and a particle shape distribution was obtained (Fig. 7). This data were then used to ensure that the same distribution between particle shapes was maintained when generating particles for the DEM model.

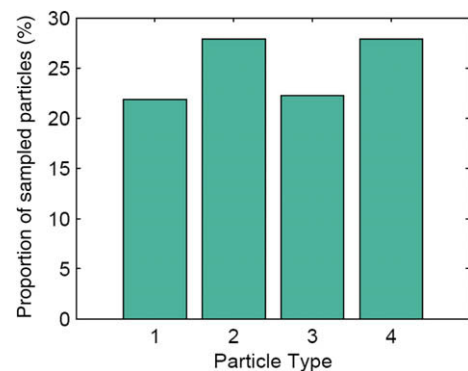


Fig. 7. Measured particle shape distribution on a random sample of 300 rocks.

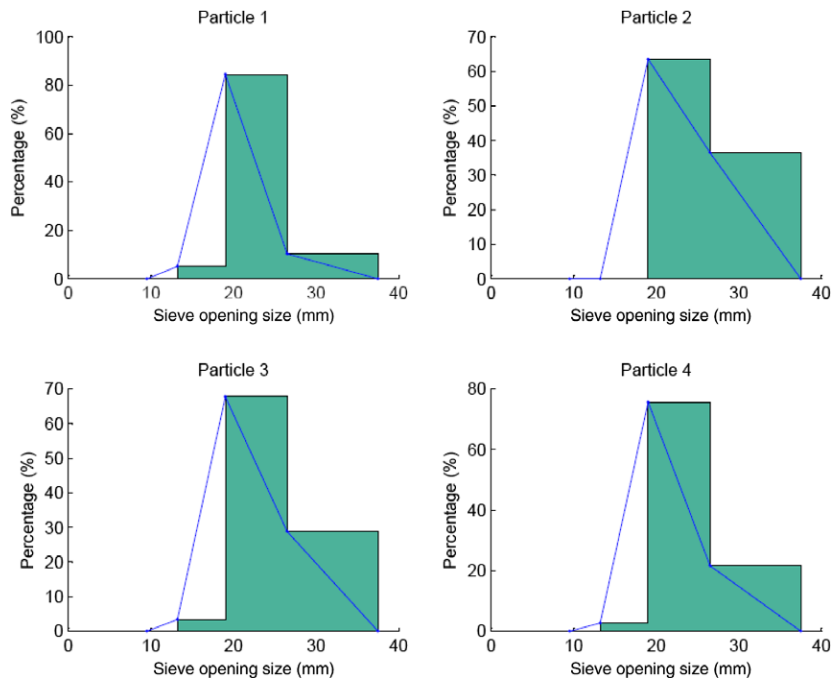


Fig. 8. Measured particle size distribution and linear distribution used in the DEM model.

4.2. Particle size distribution

A sample of each particle shape was taken and the size distribution obtained using a sieve set (mesh sizes of 9.5, 13.2, 19, 26.5, 37.5 mm). The results can be seen in Fig. 8 for each particle shape. A *MATLAB* code was written to generate clumps using the particle shape distribution and the particle size distribution. The sorting sieve classifies the particles in discrete sizes, and the distribution between these sizes was assumed to be linear. In (Fig. 8), the linear distribution used to generate the clumps can be seen.

4.3. Particle and bulk density

A container with known volume was filled with a rock sample. The sample was weighed and divided by the volume of the container to obtain the bulk density. An identical container was generated numerically in *PFC^{3D}*. Particles with the previously determined shape and size distribution were then generated and allowed to fill the container. Once the particles had settled under gravity, the mass of the particles occupying the container was calculated together with the occupied volume. The density of the particles was then adjusted using the ratio of the measured bulk density to the numerically calculated bulk density. The system was allowed to reach static equilibrium and the process was repeated until the measured bulk density was achieved. Within three to four iterations, an accuracy of 0.1% could be achieved.

Note that the resultant particle density is not necessarily the same as the solid rock density. The particle size and shape distributions are already determined and only the

bulk density is matched. In future, both the bulk density and the solid particle density will be used in calibration procedures. This will mean that the material porosity will be more accurately modelled which may improve results.

4.4. Normal and shear stiffness

In the confined compression test (also called the oedometer test), stress is applied to the specimen along the vertical axis, while strain in the horizontal directions is prevented. Shear stresses and shear strains as well as compressive stresses and volume changes occur in this test, but since the material is prevented from failing in shear, compression is the dominant source of strain. Usually this test is used to determine soil consolidation ratios. Here it is used to determine the elastic stiffness of the material, similar to a uniaxial tensile test. A cylindrical container with a diameter of 400 mm was filled with rock to a height of approximately 250 mm. A compression load was applied to the lid. The load was measured using a load cell and the axial displacement was measured using a linear variable differential transducer (LVDT). A MTS machine was used to apply the compression load.

The system was slowly loaded, unloaded and reloaded and the force-displacement curves were recorded as shown in Fig. 9. After three to four loading-unloading cycles, a stable hysteresis loop was obtained with the slope of the loading curve the same for each cycle. The stiffness was defined as the gradient of the loading curve between two points as shown in Fig. 9. The process was repeated numerically, and the stiffness compared to the measured stiffness. It was found that the particle friction coefficient had no significant effect on

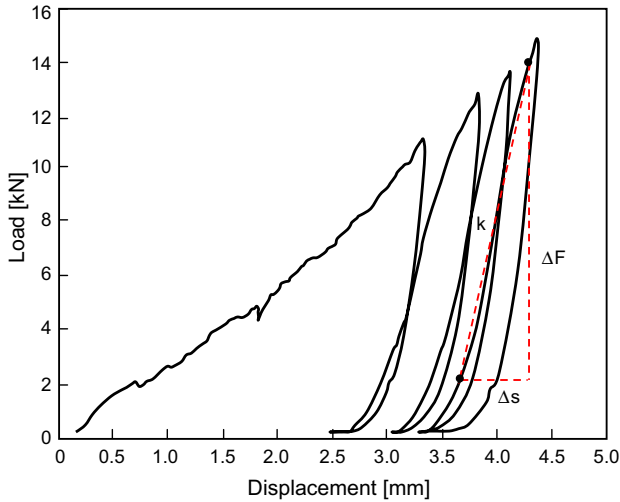


Fig. 9. Typical oedometer load-displacement curve.

the numerical oedometer results, and that the particle stiffness is the only unknown parameter with a major influence on the results. The measured bulk stiffness was numerically matched by changing the particle stiffness.

4.5. Friction

The internal friction is comprised of two components, namely, the particle interlocking and the contact friction between individual particles. The particle interlocking is affected by the particle shapes and size distribution. The friction coefficient can be calibrated using an angle of repose simulation. It is known that for frictional cohesionless granular material, the angle of repose is a good indication of the internal friction angle ([16]).

A sample of the material was taken and dropped from a given height through a funnel with a known diameter. This process was continued until a given mass of material had been allowed to flow through the funnel. The angle of repose was then measured to be 41° (Fig. 4).

The dimension of the experimental setup was then used to construct an identical numerical model. The same mass of material was allowed to flow through the funnel and the angle generated was measured. This process was continued, varying the inter-particle friction coefficient, until the same angle was obtained.

4.6. Summary of material properties

The particle shape and size was based on direct measurements and observations. Initial values for the particle stiffness and friction were estimated. It was found that the oedometer test was not significantly influenced by the friction value, but depended mainly on the particle stiffness. From this test, a value for the particle stiffness could be obtained. The stiffness values had a minor influence on the angle of repose simulation while the friction value was an important parameter. With the stiffness known

Table 1

Calibrated material properties.

Parameter	Value
Particle density ρ	1518 kg/m ³
Normal stiffness k_n	1.75×10^7 N/m
Shear stiffness k_s	1.75×10^7 N/m
Friction coefficient μ	0.53

from the oedometer simulation, the angle of repose test could be used to determine the particle friction value.

If one parameter is changed, all the other parameters need to be re-calibrated to some extent. The particle shape and size were kept constant, and two iterations were used to determine final values for the particle density, particle stiffness and particle friction coefficient (Table 1). Note that the shear stiffness is assumed to have the same value as the normal stiffness. This is an assumption often made in discrete element modelling [15] since it is very difficult to measure the shear stiffness independent from the normal stiffness.

5. Bucket dynamic model

PFC^{3D} has two main element types, namely, walls and balls (spheres). The balls are used to simulate the granular materials and the walls are used to simulated rigid bodies. PFC^{3D} is a command-based solver that relies on the user to define the simulation setup and parameters. Built into the solver is a programming language called FISH, which can be used to control and/or modify the simulation in real-time.

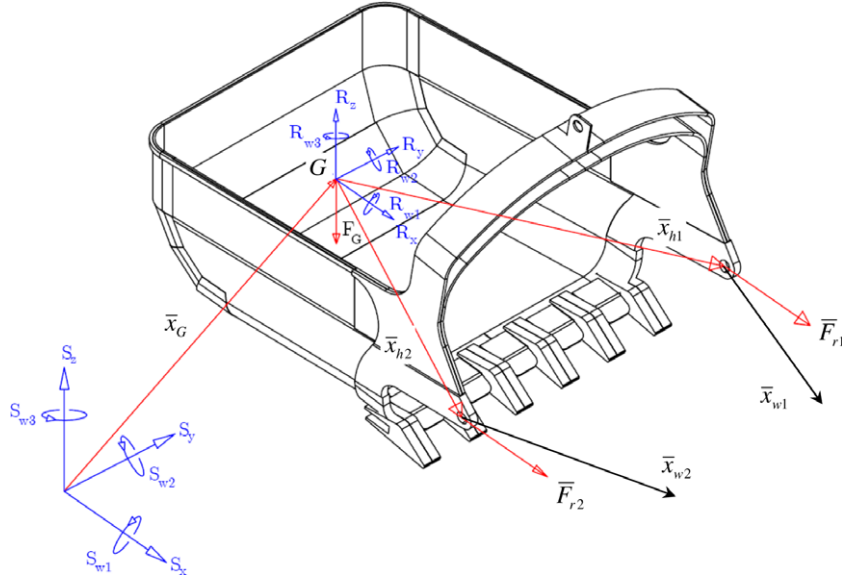
PFC^{3D} does not solve the equations of motion for the walls. Walls can only be given a constant velocity (translation and rotation around a specified axis. The velocity of each wall, can however be updated every time step using FISH functions. The basic formulation used in this algorithm is given below.

Define the global or static coordinate system as S . In order to simplify the formulation, a second rotating coordinate system R is attached to the centre-of-gravity (point G) of the bucket and aligned with the principal axes, Fig. 10. The rotation matrix from base S to R is defined as \bar{E}_S^R and vice versa. FISH has built-in functions that can be used to obtain the resultant force \bar{F}_{iS} and resultant moment \bar{M}_{iS} acting on wall i due to particle contact forces. The dynamics program uses these forces and moments, together with the physical properties of the bucket, to update the bucket's velocity in base S .

The velocity vector $\dot{\bar{x}}_{pS}$ of any point p on the bucket can be written in the static coordinate system as,

$$\dot{\bar{x}}_{pS} = \dot{\bar{x}}_{GS} + \bar{E}_R^S (\bar{\omega}_{GR} \times \bar{x}_{pR}) \quad (3)$$

where $\dot{\bar{x}}_{GS}$ is the velocity vector of the bucket's centre-of-gravity in base S , $\bar{\omega}_{GR}$ the bucket's rotational velocity vector in base R and \bar{x}_{pR} the position vector of point p relative to G in base R .


 Fig. 10. Static coordinate systems S and rotating coordinate system R attached to the bucket's centre-of-gravity.

The acceleration of the bucket's centre-of-gravity at time t is given by,

$$\ddot{\bar{x}}_{GS}^t = \frac{\sum_{i=1}^N \bar{F}_{iS}^t + \bar{F}_{r1S}^t + \bar{F}_{r2S}^t + \bar{F}_{GS}^t}{\sum_{i=1}^N m_i} \quad (4)$$

where N is the number of walls making up the bucket and m_i the mass of wall i , \bar{F}_{r1S}^t and \bar{F}_{r2S}^t are the forces acting on the bucket due to the two drag ropes, respectively, \bar{F}_{GS}^t is the body force. The expressions for the rope forces are given in Eq. (20). Using an explicit approximation, the bucket's centre-of-gravity velocity at time $t + \Delta t$ is given by

$$\dot{\bar{x}}_{GS}^{t+\Delta t} = \dot{\bar{x}}_{GS}^t + \ddot{\bar{x}}_{GS}^t \Delta t \quad (5)$$

The rotational acceleration can be written as

$$\dot{\bar{\omega}}_{GR}^t = \bar{M}_R^t + \bar{I} \begin{bmatrix} I_{[2,2]} - I_{[3,3]} \omega_{R[2]}^t \omega_{R[3]}^t \\ I_{[3,3]} - I_{[1,1]} \omega_{R[1]}^t \omega_{R[3]}^t \\ I_{[1,1]} - I_{[2,2]} \omega_{R[1]}^t \omega_{R[2]}^t \end{bmatrix} \quad (6)$$

with $\bar{M}_R^t = \bar{E}_S^{Rt} (\sum_{i=1}^N \bar{M}_{iS}^t + \bar{F}_{r1S}^t \times \bar{x}_{h1S}^t + \bar{F}_{r2S}^t \times \bar{x}_{h2S}^t)$ the resultant moment acting on the bucket and

$$\bar{I} = \begin{bmatrix} 1/I_{[1,1]} & 0 & 0 \\ 0 & 1/I_{[2,2]} & 0 \\ 0 & 0 & 1/I_{[3,3]} \end{bmatrix} \quad (7)$$

With $I_{[1,1]}$, $I_{[2,2]}$, $I_{[3,3]}$ the diagonal entries of the bucket's inertial matrix and \bar{x}_{h1} and \bar{x}_{h2} the position vector in base S of the hitch points (points on the bucket where the drag chains/ropes are connected) relative to the bucket's centre-of-gravity G . The rotational velocity $\bar{\omega}_{GR}^{t+\Delta t}$ at time $t + \Delta t$ is given using an explicit approximation

$$\bar{\omega}_{GR}^{t+\Delta t} = \bar{\omega}_{GR}^t + \dot{\bar{\omega}}_{GR}^{t+\Delta t} \Delta t \quad (8)$$

The rotational matrix \bar{E}_S^R can be written in quaternion form as

$$\bar{E}_S^R = \begin{bmatrix} 2\rho_{[0]}^2 + 2\rho_{[1]}^2 - 1 & 2(\rho_{[1]}\rho_{[2]} - \rho_{[3]}\rho_{[0]}) & 2(\rho_{[1]}\rho_{[3]} - \rho_{[2]}\rho_{[0]}) \\ 2(\rho_{[1]}\rho_{[2]} - \rho_{[3]}\rho_{[0]}) & 2\rho_{[0]}^2 + 2\rho_{[2]}^2 - 1 & 2(\rho_{[2]}\rho_{[3]} - \rho_{[1]}\rho_{[0]}) \\ 2(\rho_{[1]}\rho_{[3]} - \rho_{[2]}\rho_{[0]}) & 2(\rho_{[2]}\rho_{[3]} - \rho_{[1]}\rho_{[0]}) & 2\rho_{[0]}^2 + 2\rho_{[3]}^2 - 1 \end{bmatrix} \quad (9)$$

with

$$\bar{\rho} = \begin{bmatrix} \rho_{[0]} \\ \rho_{[1]} \\ \rho_{[2]} \\ \rho_{[3]} \end{bmatrix} = \begin{bmatrix} \sin \frac{\phi}{2} \\ \bar{a} \cos \frac{\phi}{2} \end{bmatrix} \quad (10)$$

and ϕ and \bar{a} being the rotation angle and rotation axis of the bucket. Using the second order integration scheme developed for this paper, $\bar{\rho}^{t+\Delta t}$ can be approximated by

$$\bar{\rho}^{t+\Delta t} = \left[\cos \left(\frac{\Delta t}{2} \omega \right) \bar{I}_d + \frac{\Delta t}{2} \sin c \left(\frac{\Delta t}{2} \omega \right) \bar{\Omega}_R^t \right] \bar{\rho}^t \quad (11)$$

where

$$\sin c(\theta) = \sin(\theta)/\theta \quad (12)$$

$$\omega = \|\omega_{GR}^t\| \quad (13)$$

$$\bar{\Omega}_R^t = \begin{bmatrix} 0 & -\omega_{GR}^t \\ \omega_{GR}^t & -\bar{\omega}_{GR}^t \end{bmatrix} \quad (14)$$

$$\bar{\omega}_{GR}^t = \begin{bmatrix} 0 & -\omega_{GR[3]}^t & \omega_{GR[2]}^t \\ \omega_{GR[3]}^t & 0 & -\omega_{GR[1]}^t \\ -\omega_{GR[2]}^t & \omega_{GR[1]}^t & 0 \end{bmatrix} \quad (15)$$

and \bar{I}_d the identity matrix. Note that ω_{GR}^t is a row vector and $\bar{\omega}_{GR}^t$ a column vector. Eq. (11) is used to calculate the quaternion at time $t + \Delta t$ which is then used in Eq. (9) to calculate the rotation matrix \bar{E}_S^R at time $t + \Delta t$.

The drag ropes were modelled as virtual ropes (steel) with a given stiffness. The ropes are attached to a winch system on the dragline and the position of the winches

relative to the bucket is known. The distance that a rope is pulled by the winch in a single time step is given by

$$\Delta L_w = V_r \Delta t \quad (16)$$

where V_r is the rope drag speed over the winch. The speed of a hitch point in base S is given by

$$\dot{\bar{x}}_{hS} = \dot{\bar{x}}_{GS} + \underline{\bar{E}}_R^S (\underline{\omega}_{GR} \times \bar{x}_{hR}) \quad (17)$$

where \bar{x}_{hR} is the position of the hitch point relative to the bucket's centre-of-gravity in base R (Fig. 10). The velocity of the hitch point is not necessarily in the direction of the drag ropes due to bucket rotation. The distance that the hitch point moves in the direction of the drag rope in a single time step is given by the dot product

$$\Delta L_h = \Delta t (\dot{\bar{x}}_{hS} \cdot \bar{x}_w) \quad (18)$$

where \bar{x}_w is the unit vector pointing from the hitch point towards the winch. The accumulated length change of the drag rope is calculated as

$$\Delta L^{t+\Delta t} = \Delta L^t + (\Delta L_w^t - \Delta L_h^t) \quad (19)$$

Using the rope stiffness k_r , the rope force is given as

$$\bar{F}_{rS}^{t+\Delta t} = \begin{cases} k_r \Delta L^t & \text{if } \Delta L^t > 0 \\ 0 & \text{if } \Delta L^t \leq 0 \end{cases} \quad (20)$$

The force in each of the two ropes is calculated independently and they can be different because of the rotation (roll and yaw) of the bucket.

6. DEM model setup

The modelling of large systems is still a challenge [25]. Even with parallel processing becoming available, clever modelling can reduce the computation times without loss in accuracy.

6.1. Drag bed design

Reducing the number of particles and walls in the model is the most obvious and most effective means of reducing computation time as it reduces the number of calculations performed at each cycle. A drag bed is considered optimised when its volume is as small as possible, without allowing

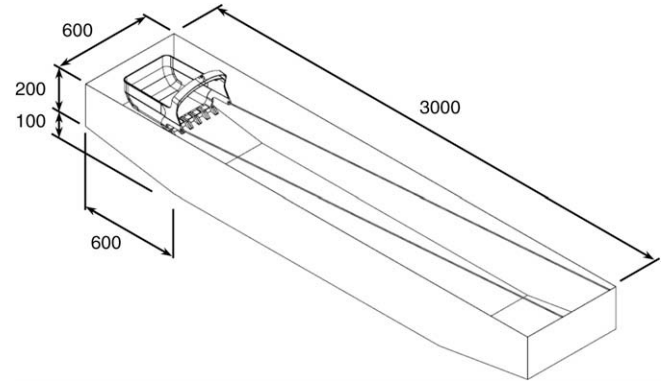


Fig. 11. Drag bed design (dimensions in mm).

boundary effects to unduly influence the simulation. Experimental data revealed that the bucket follows a parabolic trajectory while filling. The drag bed was modelled using this information and simplified to reduce the number of balls. The drag bed can be seen in Fig. 11. This shape requires 25% less particles than a standard rectangular drag bed, assuming that the particle geometry remains constant.

6.2. Bucket design

A CAD model of the bucket was created and converted to a STL (stereolithography) model. In a STL model, all surfaces are defined by unstructured triangles. A code was written to change the STL model to PFC^{3D} wall commands. In order to decrease the total number of walls, the bucket was simplified in the following ways:

- rounds or fillets were replaced with chamfers or completely removed,
- the bucket basket was given a uniform thickness,
- the arch and top rail were removed and,
- the small gap that normally exists between the teeth and the shrouds, (Fig. 12) was eliminated.

The simplifications were restricted to areas that would have little or no effect on the flow of material in or around the bucket. The simplified bucket shape can be seen in Fig. 12. The new bucket allowed the number of walls to

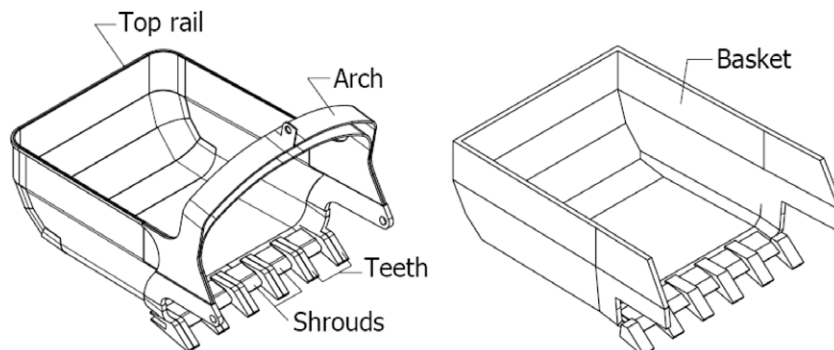


Fig. 12. Original bucket and the simplified design.

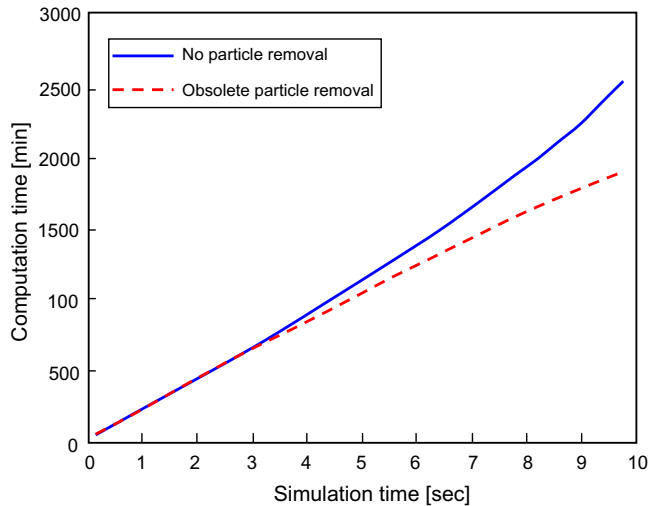


Fig. 13. The effect of removing obsolete particles on computation time.

be reduced from 5000 to 520. Although these changes would affect the bucket weight and moments of inertia, the original weight and moments of inertia were used in the dynamic bucket model.

6.3. Obsolete particle removal

The particles behind the bucket no longer have any real effect on the simulation. These particles can be removed to decrease the total number of particles and decrease the cycle time. At certain intervals, all the particles more than one bucket length behind the bucket were removed and the last row of remaining particles fixed to form a retaining wall.

The results can be seen in Fig. 13. As particles are removed, the computation time is reduced compared to the original simulation where all the particles were kept. At the end of the simulation, the total computational time saved is roughly 30%. In order to make sure that the removal of particles does not influence the bucket, the position of the bucket's centre-of-gravity and the pitch angle were plotted versus drag distance in Fig. 14. The bucket depth is the position of the bucket's centre-of-gravity perpendicular to the drag bed. From the results it is clear that removing particles more than one bucket length behind the bucket has no significant influence on the bucket's motion.

7. Bucket filling

Each experiment was repeated three times to ensure the results were reliable and repeatable. The bucket position, orientation and drag force were recorded for each test. The results showed that the bucket behaviour is predominantly two-dimensional with very little rolling and yawing motion. [23] also observed that the flow of material into the bucket is mostly two-dimensional and the motion of a dragline bucket can be accurately modelled taking into account only the bucket translation in the drag direction,

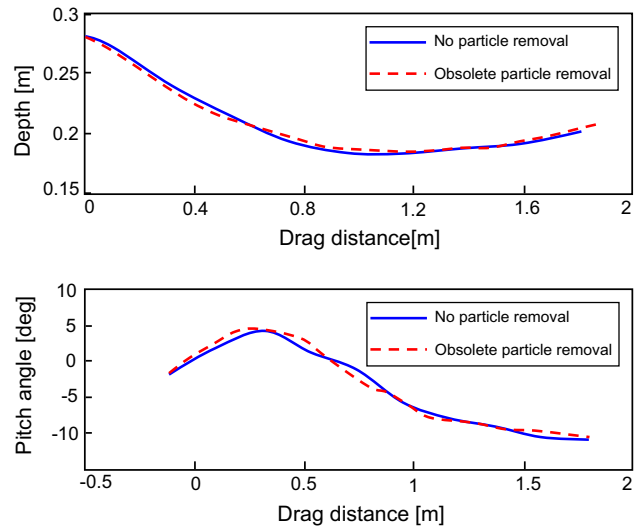


Fig. 14. The effect of removing obsolete particles on the bucket depth and pitch angle.

translation vertical to the drag direction as the bucket digs into the soil and pitching.

Tests were done at drag speeds of 0.1–0.2 m/s. Results show that there is a very small increase in drag force with an increase in speed. This can be attributed to the dynamic effects and has been observed during other soil-implement interactions [18].

Fig. 15 shows the bucket's pitch angle versus drag distance. In both the experiment and the simulation, the bucket was placed flat on the drag bed and the pitch angle set to zero. During the experiment, the pitch angle increased to almost 3° before it decreased as the bucket started to dig into the soil. At a displacement of roughly 0.3 m (one bucket length), the pitch angle has decreased to -6.5° . The DEM model also predicts this behaviour with the pitch angle at -10° after a displacement of one bucket length.

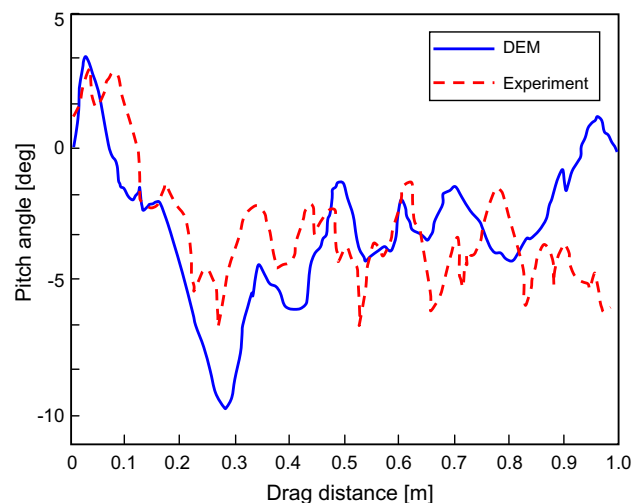


Fig. 15. Comparison between the measured and the DEM predicted pitch angle.

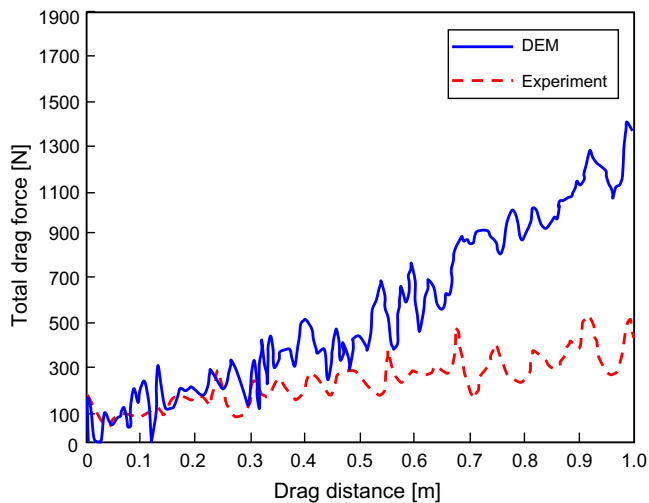


Fig. 16. Comparison between the measured and the DEM predicted drag force.

Fig. 16 shows the total drag force (sum of the force in each of the two drag ropes) versus drag distance. There is almost linear increase in measured drag force with a final value of 500 N at a drag distance of 1 m (three bucket lengths). The DEM model accurately predicts the drag force up to a displacement of 0.3 m (one bucket length). Thereafter, DEM predicts higher drag forces and at the end of the drag it is almost three times the measured value. The reason for this is not fully understood. One of the reasons might be the fact that the porosity of the material changes as it is disturbed by the bucket. Material porosity was not included in the calibration process, so the porosity changes in the model might differ from the porosity changes in the real material. Porosity measurements will be included in future studies and in the calibration process.

Fig. 17 illustrates one of the advantages of DEM simulations where the mass of material inside the bucket can easily be determined as a function of drag distance. A

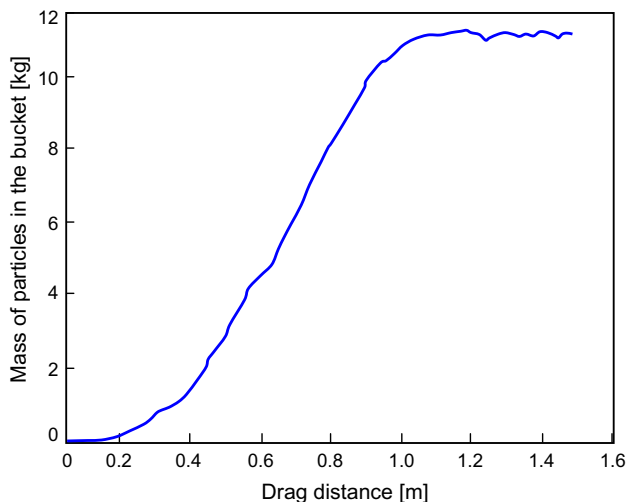


Fig. 17. The DEM predicted soil mass inside the bucket.

FISH function was written which checked all particles and simply added up the mass of all particles found to be inside the bucket. This can easily be done since the position and orientation of the bucket is known. It is difficult to verify this experimentally since it is difficult to determine the mass of material inside the bucket without influencing the experiment. This result also confirms that the bucket fills within 3 bucket lengths (1 m in drag distance), a rule of thumb used by bucket manufacturers [26].

8. Conclusion

A procedure to determine the micro parameter values for the DEM modelling of cohesionless granular material was presented. The particle size, shape and density were directly measured and modelled. The particle stiffness and friction coefficient were determined by confined compression tests and angle of repose tests. It was found that the compression test is mainly dependent on the particle stiffness and the particle friction coefficient had no significant effect on the results. From this test, the particle stiffness could be determined. Thereafter, the angle of repose test could be used to determine the particle friction coefficient.

It is shown that a saving of up to 30% in computation time can be achieved by removing (deleting) obsolete particles. Particles more than one bucket length behind the bucket were removed without affecting the motion of the bucket.

The experiments showed that the motion of a dragline bucket is mainly two-dimensional. The bucket yaw and roll is very small compared to the pitch. The translation of the bucket is mainly in the direction of the drag and perpendicular to the drag direction (digging into the soil). Transverse motion was found to be minimal.

It is shown that DEM can accurately predict the bucket orientation. DEM can also predict the drag force during the first third of the drag distance. During later stages of the drag, DEM predicts drag forces that are too high. It is shown that DEM can be used to predict the bucket fill rate with a fill distance of approximately 3 bucket lengths, a figure found in literature [23] and in industry.

A further sensitivity study is needed to determine the influence of the DEM parameters (such as particle stiffness and friction) on the bucket filling results. A preliminary study has shown that the particle stiffness has an influence on the vertical motion of the bucket. With a decrease in particle stiffness the bucket dives deeper into the material.

References

- [1] Advanced Conveyor Technologies. Available from: <http://www.ac-tek.com>; 2008 [accessed 21.04.08].
- [2] Applied DEM. Available from: <http://www.applieddem.com>.
- [3] Asaf Z, Rubinstein D, Shmulevich I. Determination of discrete element model parameters using in-situ tests and inverse solution techniques. Proceedings of the 15th international conference of the ISTVS, Hayama, Japan, September 25–29; 2005.

- [4] Chute Maven. Available from: <http://www.chutemaven.com>; 2008 [accessed 21.04.08].
- [5] Cleary PW, Sawley ML. Three-dimensional modelling of industrial granular flows. Second international conference on CFD in the minerals and process industries; 1999. p. 95–100.
- [6] Cleary PW. The filling of dragline buckets. *Math Eng Indus* 1998;7(1):1–24.
- [7] Cundall PA, Strack ODL. A discrete numerical model for granular assemblies. *Géotechnique* 1979;29(1):47–65.
- [8] Dayawansa P, Chitty G, Kerezi B, Bartosiewicz H, Price JWH. Fracture mechanics of mining dragline booms. *Engineering Failure Analysis* 2006;13:716–25.
- [9] DEM Solutions. Available from: <http://www.dem-solutions.com>; 2008 [accessed 21.04.08].
- [10] Esterhuysen SWP. The influence of geometry on dragline bucket filling performance. Msc Thesis Mechanical Engineering, University of Stellenbosch, Stellenbosch, South Africa; 1997.
- [11] Franco Y, Rubinstein D, Shmulevich I. Determination of discrete element model parameters for soil-bulldozer blade interaction. Proceedings of the 15th international conference of the ISTVS, Hayama, Japan, September 25–29; 2005.
- [12] Hertz H. J. *fur die reine u. angew. Math* 1882;92(136).
- [13] Hogue C. Shape representation and contact detection for discrete element simulations of arbitrary geometries. *Eng Comput* 1998;15(3): 374–90.
- [14] Itasca. Available from: <http://www.itasca.com>; 2008 [accessed 21.04.08].
- [15] Itasca. PFC^{3D}, Particle flow code in three dimensions, User's guide. 2nd ed.; 2003.
- [16] Lambe TW, Whitman RV. Soil mechanics. New York: John Wiley & Sons, Inc.; 1969.
- [17] Landry H, Lague C, Roberge M. Discrete element modelling of machine manure interactions. *Comput Electron Agric* 2006;52:90–106.
- [18] McKyes E. Soil cutting and tillage. Amsterdam: Elsevier; 1985.
- [19] Mindlin RD, Deresiewicz H. Elastic spheres in contact under varying oblique forces. *Trans ASME E J Appl Mech* 1953;20:327.
- [20] Overland Conveyor Company. Available from: <http://www.overland-conveyor.com>; 2008 [accessed 21.04.08].
- [21] Poschel T, Saluena C, Schwager T. Scaling properties of granular materials. *Phys Rev E* 2001a;(64).
- [22] Poschel T, Saluena C, Schwager T. Scaling properties of granular materials. In: Vermeer PA, Diebels S, Ehlers W, Herrmann HJ, Luding S, Ramm E, editors. Continuous and discontinuous modelling of cohesive frictional materials. Berlin: Springer; 2001. p. 173–84.
- [23] Rowlands JC. Dragline bucket filling. Phd Thesis, University of Queensland, Queensland, Australia; 1991.
- [24] Rockfield Software Ltd. Available from: <http://www.rockfield.co.uk>; 2008 [accessed 21.04.08].
- [25] Tijsskens B, Van Besin, Vandewalle, Ramon. Large scale DEM. CHoPS-05. Sorrento; 2006.
- [26] VR Steel. Available from: <http://www.vrsteel.co.za>; 2008 [accessed 21.04.08].
- [27] Walton OR, Braun RL. Viscosity, granular-temperature, and stress calculations for shearing assemblies of inelastic frictions discs. *J Reol* 1986;30(5):949–80.
- [28] Zhang D, Whiten WJ. The calculation of contact forces between particles using spring and damping models. *Powder Technol* 1996;88: 59–64.